星形成ゼミ

2015/5/29(土)

藤井浩介

SFN #268 41-45

Index

41: Stellar Multiplicity and Debris Disks: An Unbiased Sample

- David R. Rodriguez et al.
- URL: http://ads.nao.ac.jp/abs/2015MNRAS.449.3160R

42: ALMA Observations of the IRDC Clump G34.43+00.24 MM3: DNC/HNC Ratio

- Takeshi Sakai et al.
- URL: http://ads.nao.ac.jp/abs/2015ApJ...803...70S

43: Imaging study of HCOOCH3 toward Orion KL

- Yusuke Sakai et al.
- URL: http://ads.nao.ac.jp/abs/2015ApJ...803...97S

44: Star formation in the filament of S254-S258 OB complex: a cluster in the process of making

- M. R. Samal et al.
- URL: http://ads.nao.ac.jp/abs/2015arXiv150309037S

45: The Environment of the Strongest Galactic Methanol Maser

- A. Sanna et al.
- URL: http://ads.nao.ac.jp/abs/2015ApJ...804L...2S

41: Stellar Multiplicity and Debris Disks: An Unbiased Sample

David R. Rodriguez et al., MNRAS, URL: http://ads.nao.ac.jp/abs/2015MNRAS.449.3160R

"DEBRIS"のサンプルを用いた、バイナリ以上環境でのdiskの性質調査。

➢ バイナリーではdiskの検出数が減少。バイナリと単一星でdiskの性質は変わらない。

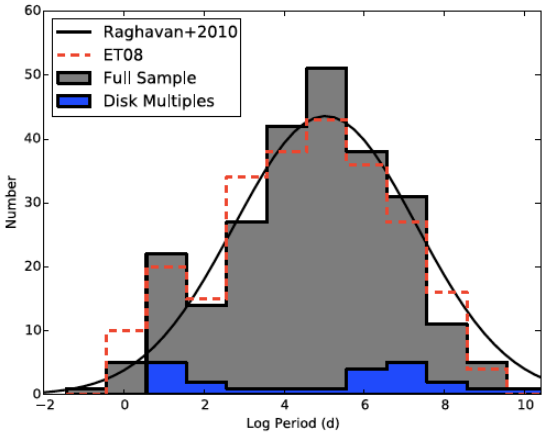

Figure 1. Distribution of calculated and measured orbital periods for multiples (grey histogram). Triples and higher order multiples have more than one period per system. The dashed line is the period distribution from Eggleton & Tokovinin (2008) and the solid curve is from Raghavan et al. (2010). Both are normalized to the number of periods in the DEBRIS sample. The blue shaded histogram shows the distribution of periods for disc-bearing multiples in our sample.

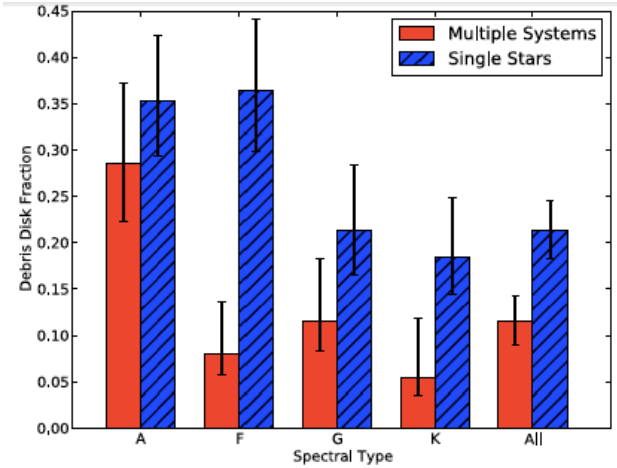

Figure 3. Disc detection frequency among the DEBRIS sample, divided by spectral type and binarity.

Herschel "DEBRIS"

- 近傍の恒星系の赤外超過を探査
- 449天体を使用
- 文献およびLick天文台のAO観測からmultiplicityを調査

① binary/multiple systemの調査

- 188のbinary/multiple systemを同定
- バイナリー周期にバイアスはない

② disk frequency(diskを有する天体の割合)の調査

- A型星ではdisk frequencyは同等
- FGK型では第二の星によりdisk frequencyが著しく低下

41: Stellar Multiplicity and Debris Disks: An Unbiased Sample

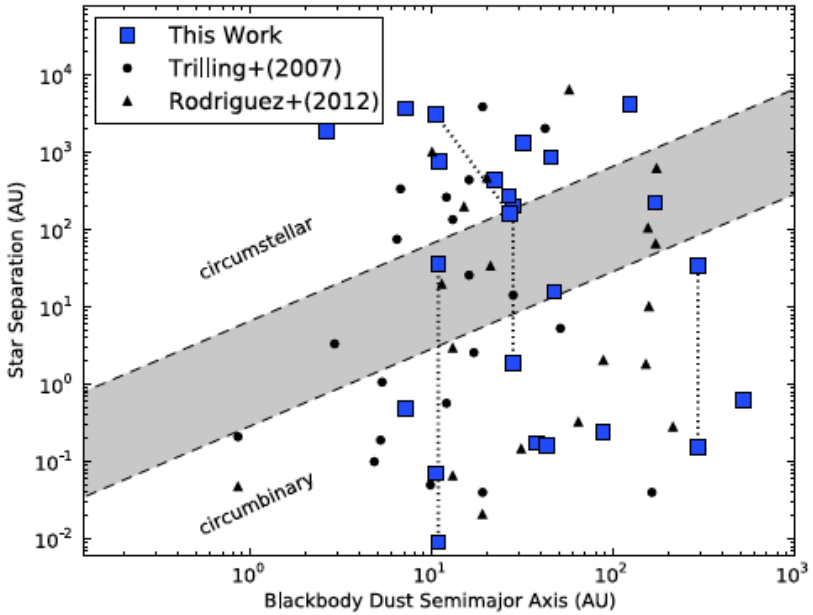

Figure 7. Stellar separation versus blackbody dust semimajor axes for the dusty multiple systems in the DEBRIS sample and from other surveys in the literature. The grey denotes the approximate region at which gravitational effects can perturb the disc. Triples where the dust lies between the AB and C pair are connected with a dotted line. HD 223352 is the system with the slanted line as the system hosts two separate debris discs. With stellar separations exceeding 150 kau, the three components of HD 216956 (Fomalhaut) are beyond the plot range in this figure.

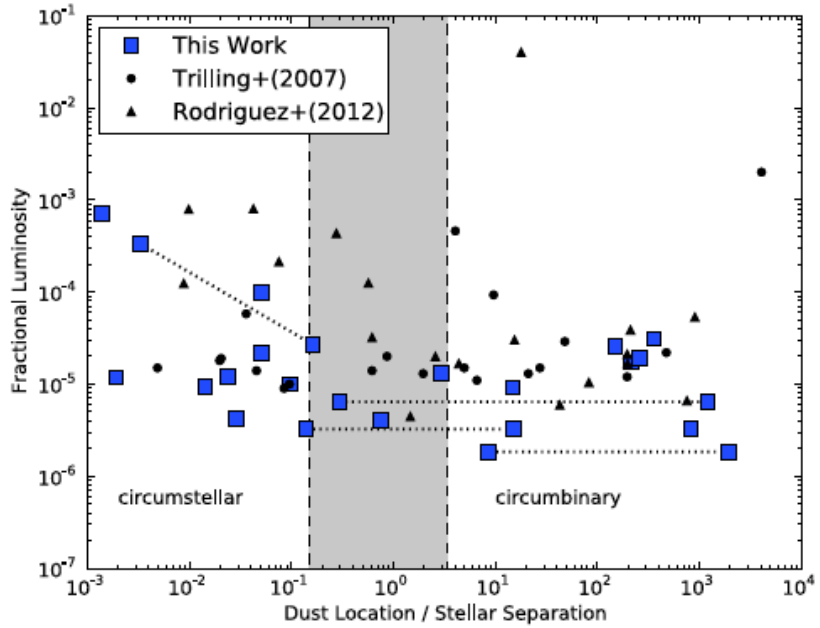

Figure 8. Ratio of dust to stellar separation compared with L_{IR}/L_* for dusty multiple systems. The grey denotes the approximate region at which gravitational effects can perturb the disc. As before, triples are connected and HD 223352 is the system connected with a slanted line as two separate debris discs are present in the system. HD 216956 (Fomalhaut) has a ratio $<10^{-3}$ and is not shown in this figure. The system with fractional luminosity ~4 per cent is BD+20 307.

③ diskの性質の違い

- ダスト温度やFractional Luminosityなど、単一星とバイナリ以上で顕著な違いはなかった

④ 結果の考察

- 伴星の重力により、diskの衝突進化が進むため、バイナリ以上でdisk frequencyが下がる
- disk形成やdiskの性質には影響しない

42: ALMA Observations of the IRDC Clump G34.43+00.24 MM3: DNC/HNC Ratio

Takeshi Sakai et al., ApJ, URL: http://ads.nao.ac.jp/abs/2015ApJ...803...70S

- ALMA Cycle 1, Band 6&7, IRDCに対するDNC, HN13C, N2H+(J=3-2)輝線観測

➢ 過去の単一鏡観測でのDNC/HNC比の違いは、dense gasのfilling factorの違いではないか

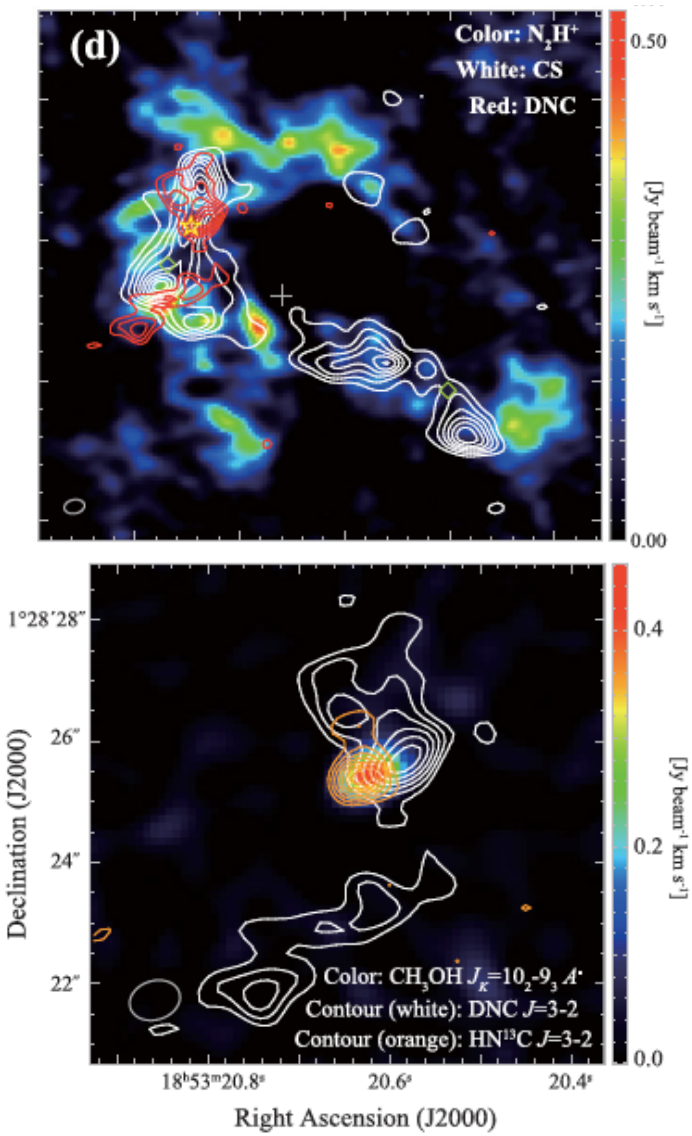

G34.43+00.24 MM3

- d~3.9 kpc, アウトフローのdynamical age < 1900yr

① CSとN2H+のanti-correlation

➢ outflow(CS)がcold gasと相互作用、N2H+を破壊する CO warm gasを形成

② Hot core(☆)周辺にDNCとHN13C

➢ Warm area(>20 K)をトレース

③ 高いN(DNC/HNC)比(average >0.06)

➢ 過去の単一鏡(J=1-0輝線、~0.003)は周囲の薄いガスを見ており、dense gasの filling factorが低かった?

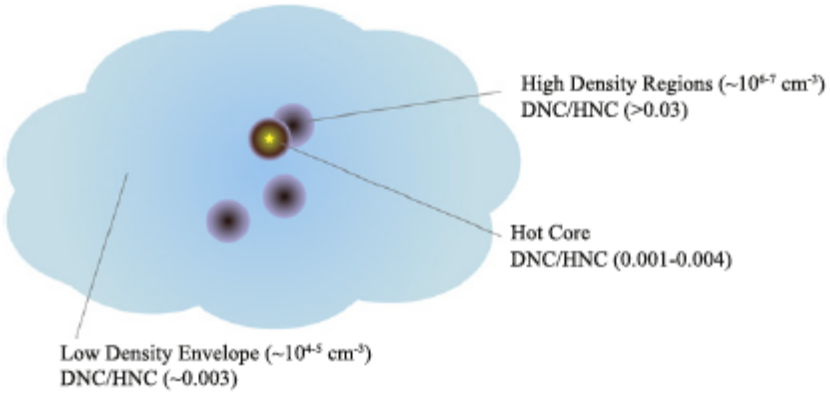

Figure 5. Schematic illustration of the distribution of the DNC/HNC abundance ratio in a clump with embedded cores.

42: ALMA Observations of the IRDC Clump G34.43+00.24 MM3: DNC/HNC Ratio

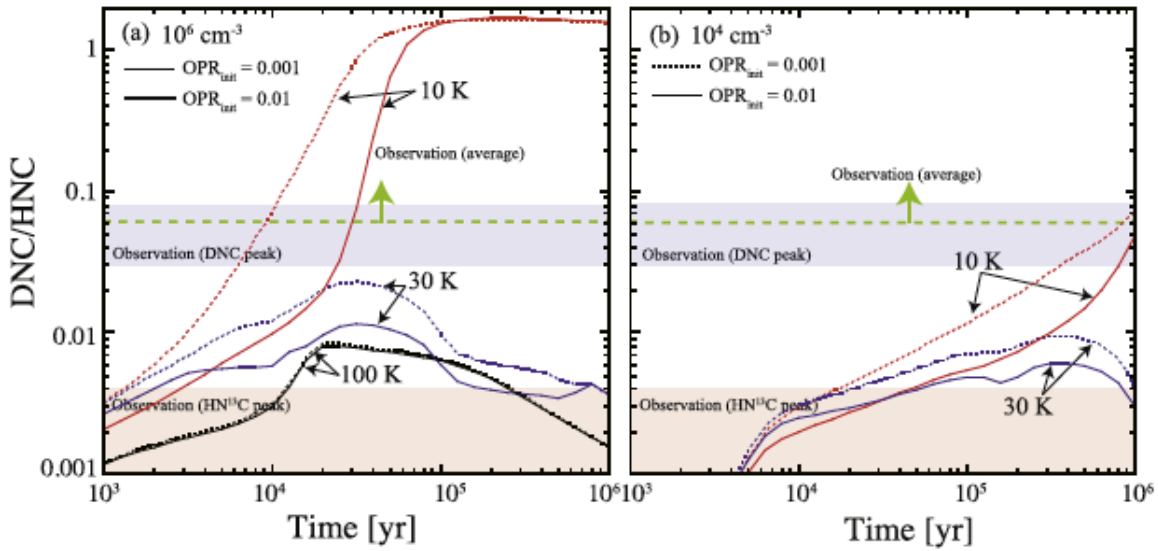

Figure 6. (a) Chemical model calculation results of the deuterium fractionation ratio of DNC/HNC assuming the constant temperatures and the constant density of 10^6 cm^{-3}. The initial o/p ratio of H_2 molecules is assumed to be 0.01 (solid lines) or 0.001 (dashed lines). The observed value for the DNC peak, the $HN^{13}C$ peak, and the average spectra is plotted as the purple region, pink region, and green dashed line, respectively. (b) Same as (a), but the density is 10^4 cm^{-3}.

④ D/H比の化学モデル計算(Furuya et al. in prep.)

- 均一温度・密度のクラウドを仮定

➢ N(DNC/HNC)比は低温・高密度ほど高くなる

⑤ DNC/HNC比総括

- high mass sourceでの低いDNC/HNC比はhigh density gas のfilling factorのせい
- high mass source間でのDNC/HNC比のバリエーションは、filling factorの違いもしくはdense regionの進化の違い

43: Imaging study of HCOOCH3 toward Orion KL

Yusuke Sakai et al., ApJ, URL: http://ads.nao.ac.jp/abs/2015ApJ...803...97S

- Orion KL, ALMA Band 6 SVデータ, 振動温度と回転温度の測定

➢ NRO45で見えていたギ酸メチルの振動温度と回転温度の違いはBeam dilutionのせいか

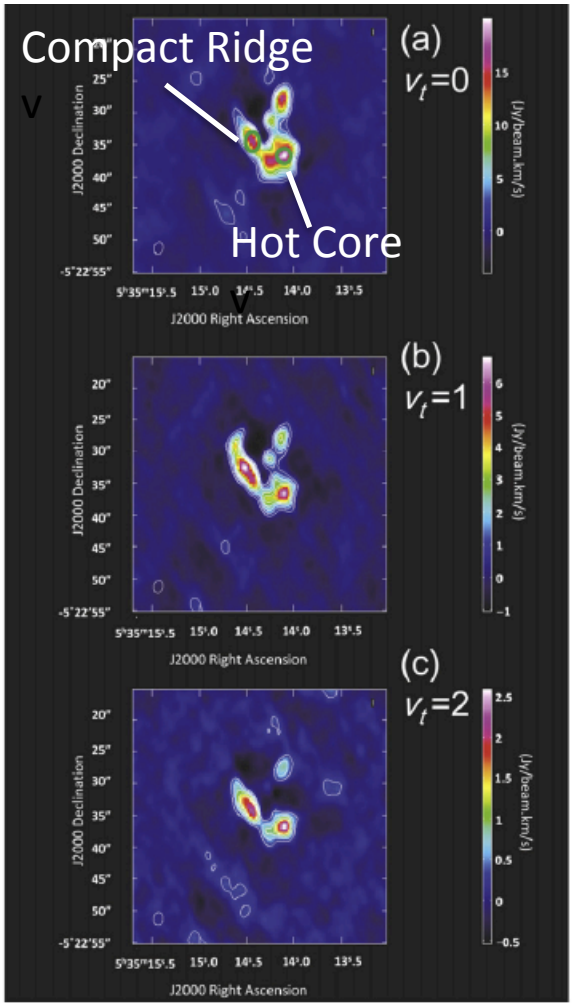

Figure 1. Integrated intensity maps of methyl formate (V_{LSR} 4–12 km s^{-1}). From top to bottom: transition of $18_{4,15}$–$17_{4,14}$ in v_t = 0, 1, and 2 at 221674 MHz (A sublevel), 219705 MHz (A sublevel) and 216594 MHz (E sublevel). The green circles shown in Figure 1(a) represent the Compact Ridge and Hot Core. The contour represents 3σ and 1σ of Figures 1(a)–(c), which are 516 mJy beam^{-1}, 204 mJy beam^{-1}, and 94 mJy beam^{-1}, respectively.

①ギ酸メチルのねじれ振動遷移輝線を同定

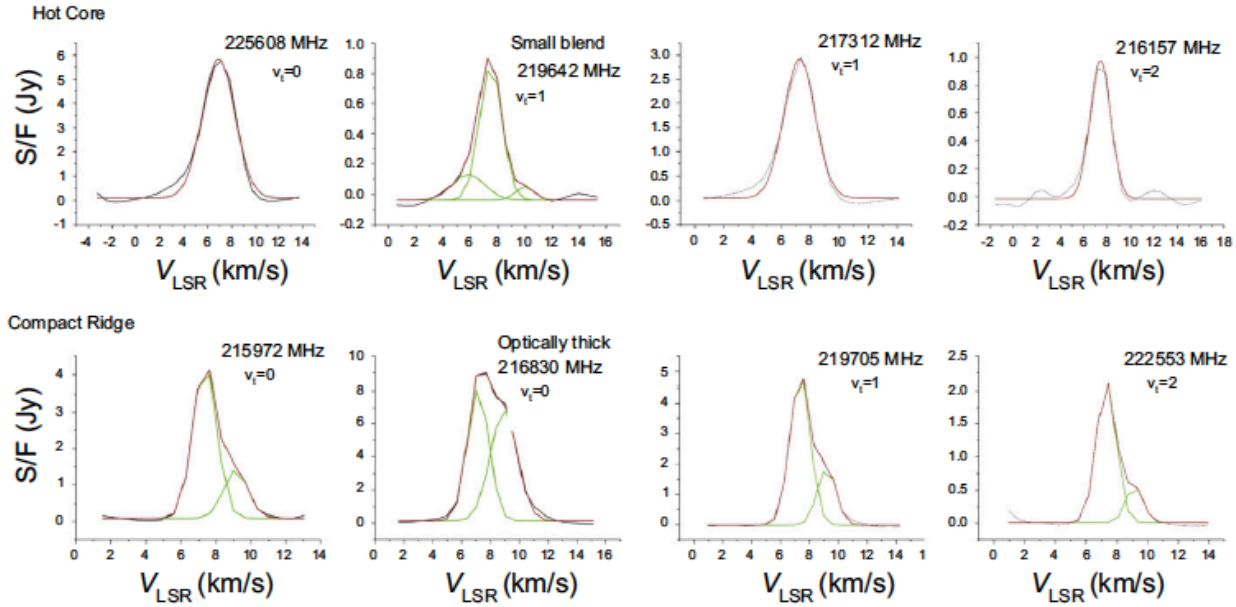

Figure 3. Examples of spectra. Green, red, and black lines represent the fitted velocity component, total, and observation. We have also modeled the contaminant in the second panel in the top left.

Table 1
Transition List for the Compact Ridge

Frequency (MHz)	v_t	J'	Ka'	Kc'	J''	Ka''	Kc''	Symmetry	$S\mu^2$ (D^2)	E_u (K)	7.3 km s^{-1} Component T (K)	FWHM (km s^{-1})	V_{LSR} (km s^{-1})	W (K km s^{-1})	9.1 km s^{-1} Component T (K)	FWHM (km s^{-1})	V_{LSR} (km s^{-1})	W (K km s^{-1})	Comments	Diagram
215972.058	0	19	1	18	18	2	17	A	7.9	145.2	38.34	1.57	7.35	64.17	12.11	1.59	9.12	20.52	NB	*
216210.859	0	19	1	18	18	1	17	E	47.5	145.2	71.31	1.78	7.16	135.06	60.04	2.23	8.92	142.34	NB	···
216830.129	0	18	2	16	17	2	15	E	44.4	143.2	72.13	1.73	7.13	133.06	60.46	2.18	8.91	140.06	NB	···
216964.812	0	20	1	20	19	1	19	E	50.8	147.2	···	···	···	···	···	···	···	···	B	···
217215.780	0	32	9	24	32	8	25	A	10.6	325.2	9.89	1.83	7.06	19.25	4.57	1.96	9.30	9.53	NB	···
218280.833	0	17	3	14	16	3	13	E	41.9	139.3	94.70	1.94	7.29	195.60	63.19	1.72	9.11	115.63	NB	···
218297.853	0	17	3	14	16	3	13	A	41.9	139.3	84.19	1.73	7.17	155.36	66.80	2.12	8.96	150.71	NB	···
218585.436	0	36	9	28	36	8	29	A	12.2	383.3	2.95	1.48	7.26	4.66	2.01	2.88	8.48	6.15	B	···
219196.154	0	36	6	30	36	6	31	E	3.4	291.1	···	···	···	···	···	···	···	···	B	···
219417.253	0	30	5	26	30	4	27	E	6.7	272.3	12.36	1.60	7.32	21.05	2.15	1.37	9.25	3.13	NB	*
219600.185	0	30	9	22	30	8	23	E	9.7	299.3	11.49	1.59	7.37	19.44	2.03	1.30	9.37	2.81	NB	···
219672.837	0	30	5	26	30	3	27	A	2.6	272.3	6.34	1.70	7.23	11.46	1.15	0.95	9.16	1.17	NB	*
220166.834	0	17	4	13	16	4	12	E	41.3	141.3	81.01	1.68	7.12	145.26	66.88	2.17	8.91	154.15	B	···
220190.216	0	17	4	13	16	4	12	A	41.3	141.3	86.31	1.69	7.16	155.51	67.67	2.05	8.93	147.38	NB	···

43: Imaging study of HCOOCH3 toward Orion KL

Table 4
Comparison of Temperatures and Column Densities of Methyl Formate

Position	T_{rot} (K) $v_t = 0$	T_{rot} (K) $v_t = 1$	T_{rot} (K) $v_t = 2$	T_{eff} (K)	N_{tot}(cm^{-2})	T_{eff}(K)[a]	N_{tot}(cm^{-2})[a]	N_{tot}(cm^{-2})[b]
Compact Ridge 7.3 km s^{-1} component	146 ± 17	153 ± 20	219 ± 56	99.6 ± 8.1	$1.11 \pm 0.31 \times 10^{18}$	79 ± 2	$1.60 \pm 0.10 \times 10^{17}$	$5\text{–}8.5 \times 10^{17}$
Compact Ridge 9.1 km s^{-1} component	82.9 ± 3.7	93 ± 14	97 ± 28	86.8 ± 4.1	$3.42 \pm 0.79 \times 10^{17}$	112 ± 50	$6.8 \pm 2.1 \times 10^{16}$	7×10^{16}
Hot Core	162 ± 26	153 ± 24	...	119.9 ± 9.2	$6.0 \pm 1.6 \times 10^{17}$	128 ± 9	$1.60 \pm 0.20 \times 10^{17}$	$3.3\text{–}4.3 \times 10^{17}$
Averaged[c]	43 ± 9	53 ± 8	...	124 ± 5	$1.38 \pm 0.14 \times 10^{16}$	...	...	...

Note. In the column header, T_{rot}, T_{eff}, and N_{tot} represent rotational temperature, effective temperature, and column density. Effective temperature is defined by using data in multiple torsional states.
[a] Favre et al. (2011).
[b] Favre et al. (2014).
[c] Takano et al. (2012).

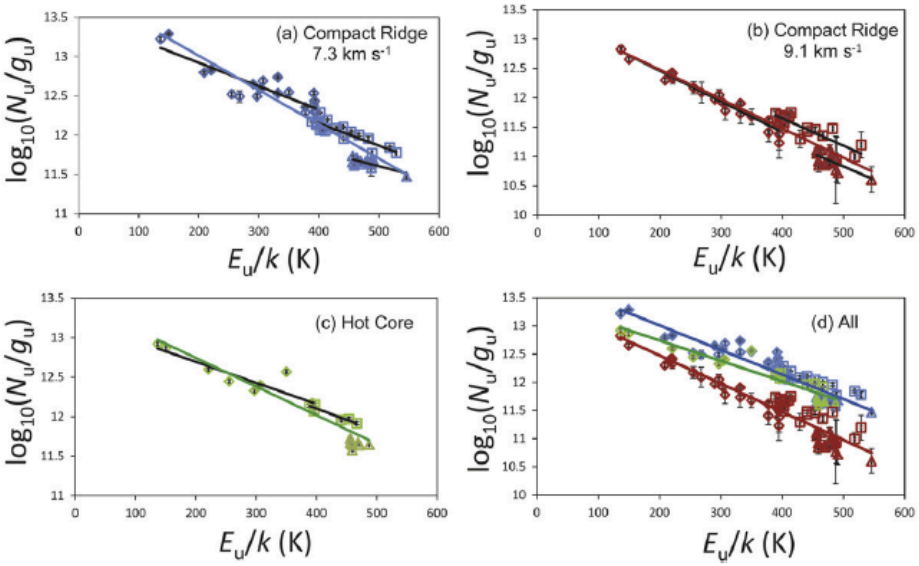

Figure 4. Rotation diagram of methyl formate at the two positions. There are two velocity components at the Compact Ridge. Blue, red, and green colors represent transitions for the Compact Ridge 7.3 km s^{-1} component, the 9.1 km s^{-1} component, and the Hot Core. The diamonds, rectangles, and triangles represent $v_t = 0$, 1, and 2, respectively. The corresponding colored lines show the least-square fitted lines to derive the effective temperatures by using all the transitions. Black colored lines were used to derive the rotational temperature of the each torsional states. The error bars were calculated from the errors of intensity of the Gaussian fit.

② rotation diagramより温度算出
Trot ~ Teff(=Tvib) @9.1 km/s
Trot > Teff(=Tvib) @7.3 km/s

Takano et al. 2012では Trot < Tvib

- 低分解能によるBeam dilution、もしくは今回のEuのレンジの狭さによる不確定性か

44: Star formation in the filament of S254-S258 OB complex: a cluster in the process of making

M. R. Samal et al., A&A submitted, URL: http://ads.nao.ac.jp/abs/2015arXiv150309037S

- MIPS, WISEのアーカイブからフィラメント状のIRDC周辺のYSOを同定

➢ Filament での星形成は重力不安定による分裂が支配的

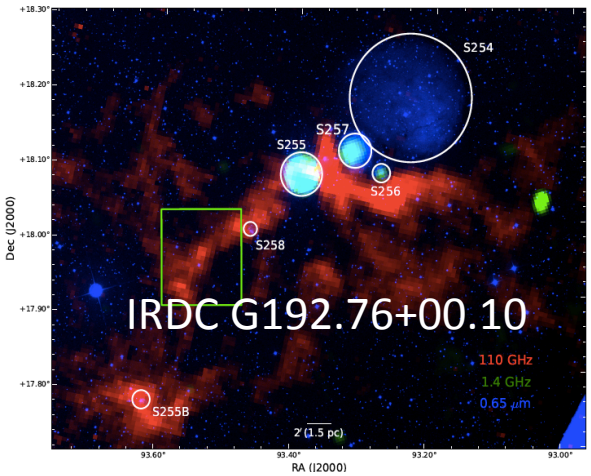

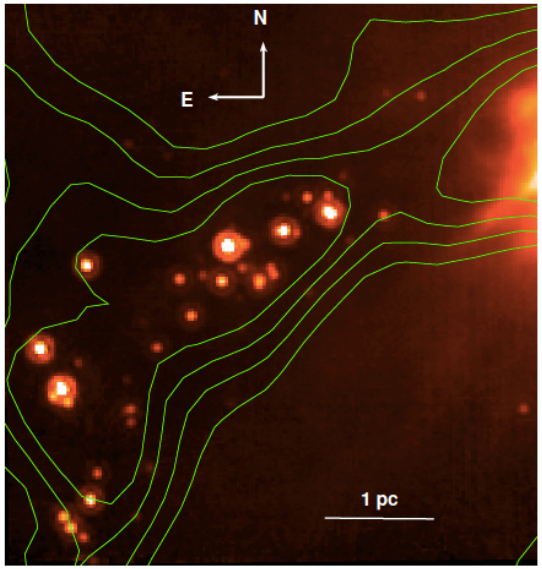

Fig. 2. *Spitzer* MIPS 24 μm image of IRDC G192.76+00.10. The image has a field of view ~7′.0 × 8′.0 centered at α_{2000} = 06^{h}13^{m}47^s, δ_{2000} = 17°54′37″ or l=192°.76, b=00°.10. The ^{13}CO column density contours are also shown (contour levels are at 0.7, 0.9, 1.1, 1.4 × 10^{16} cm^{-2}).

IRDC G192.76+00.10

- d~2.5kpc
- 5.7 pc x 1.9 pc
- isolated from feedback

① 24um, K-band点源の同定、YSOの同定、分類

- [3.4] / [3.4]-[24] diagram
- WISEデータのspectrum index
- k-[3.4]/[3.4]-[4.6] diagram

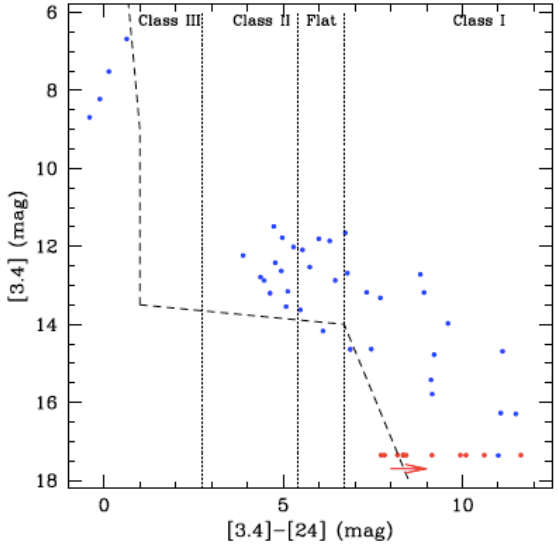

Fig. 3. The [3.4] - [24] vs. [3.4] colour-magnitude diagram for the detected MIPS 24 μm sources. The dotted lines separate the regions of Class I, Flat-spectrum, Class II, and Class III objects. The dashed lines denote the dividing line between the region occupied by contaminated sources (galaxies and disk-less stars) and YSOs (see also Rebull et al 2011). The sources for which we do not have WISE 3.4 μm detection are represented in red. For these sources, we consider the magnitude of the faintest 3.4 μm counterpart of our 24 μm detections as an upper limit. The arrow represents the direction of their colours, thus they are likely to be Class I YSOs.

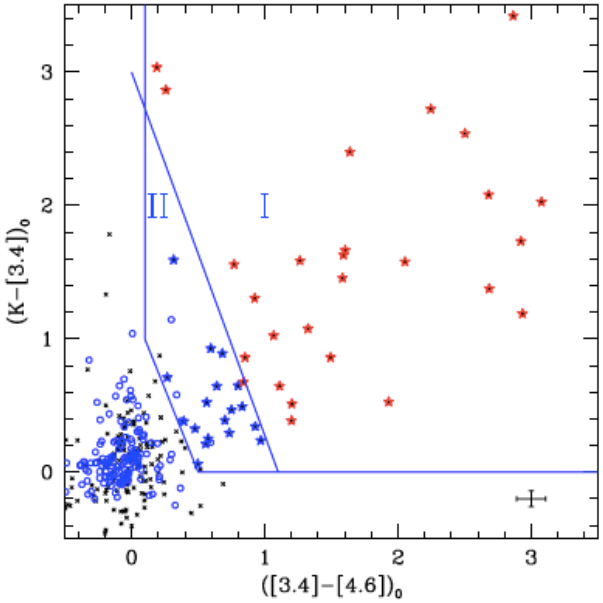

Fig. 4. Intrinsic K - [3.4] vs. [3.4] - [4.6] colour-colour diagram showing the distribution of field stars/MS sources (cross symbols), Class II YSOs (blue stars) and Class I YSOs (red stars). Slanted line indicates the boundary between the Class I and Class II YSOs. The control field sources are marked with open circles. The error bars in the bottom right corner show average errors in the colours.

44: Star formation in the filament of S254-S258 OB complex: a cluster in the process of making

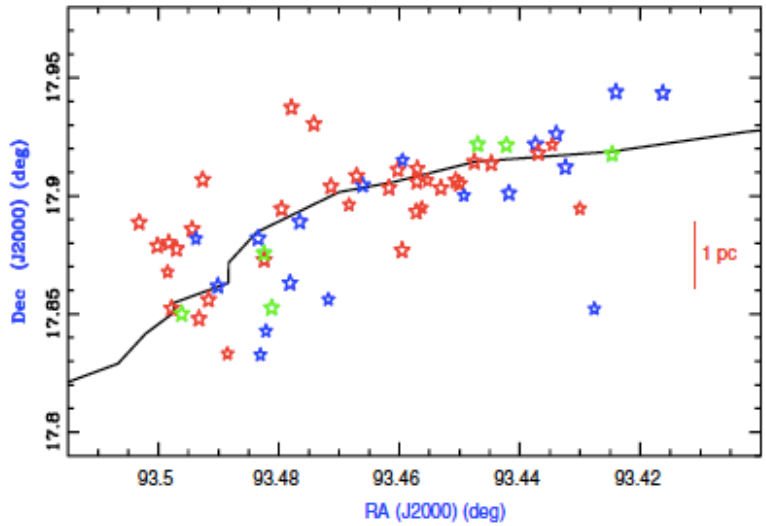

Fig. 7. The spatial distribution of Class I (red stars), Flat-spectrum-spectrum (green stars), and Class II (blue stars) YSOs. The continuous line running from south-east to north-west marks the highest H_2 column density line of the filament along its long axis.

tation, given by Hartmann (2002). In the model of Hartmann (2002), the fragmentation length (λ_c) of a cylinder due to gravitational instability is given by:

$$\lambda_c = 3.94\, c_s^2/(G\Sigma) = 1.5\, T_{10}\, A_V^{-1}\ \mathrm{pc} \quad (1)$$

where, A_V is the visual extinction corresponding to the surface density (Σ) through the center of the filament and T_{10} is the gas temperature in units of 10 K. The corresponding collapse timescale is given by:

$$\tau \sim 3.7\, T_{10}^{1/2}\, A_V^{-1}\ \mathrm{Myr}. \quad (2)$$

Herschel estimates of dust temperatures indicate that the temperature of the quiescent and star-forming filaments are in the range of 10 K to 15 K (Arzoumanian et al. 2011). Observations of the ammonia (1, 1) and (2, 2) inversion transitions suggest that the kinetic temperature in the dense part of the IRDC G192.76+00.10 filament is in the range of 13 to 15 K (Dunham et al. 2010). Considering 14 K as the temperature of the filament and 10 mag as the mean visual extinction, the above equation predicts $\lambda_c \sim 0.21$ pc and $\tau \sim 0.45$ Myr. For randomly oriented filament, the line of sight median inclination angle could be ~ 60° (Genzel & Stutzki 1989). If this is the case, then this would

② フィラメントに沿ったYSO分布
- 近いもので0.2pc間隔
- シリンダーの重力不安定波長で説明可、フィラメントのフラグメンテーションか

③ 原始星/Class2 比が高い(~2)
- 領域は約1Myrより若い

④ IRDC gas mass ~ 1100 Mo (13COより)
YSO total mass ~ 30Mo
- SFE~0.03
- 1Myrでできたとすると 、
SFR ~30 Mo/Myr ~3 Mo/Myr/pc^2
あと数Myrでクラスターになり得る

45:The Environment of the Strongest Galactic Methanol Maser

A. Sanna et al., ApJ Letters, URL: http://ads.nao.ac.jp/abs/2015ApJ...804L...2S

VLBA, LBA, JVLAによる大質量形成コアのメーザー観測研究

➢ 周期的メーザーは膨れた原始星のIR光によるものである

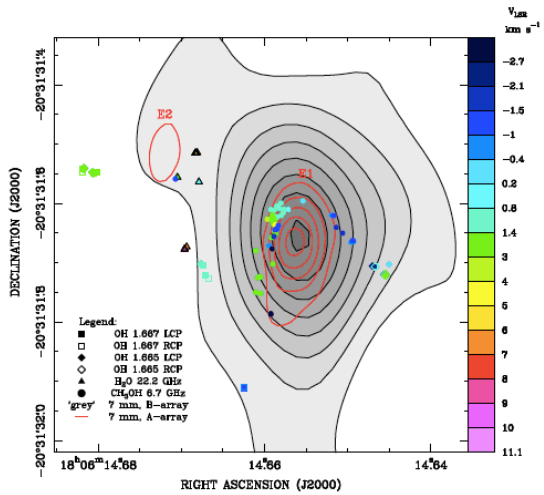

Figure 1. Combination of the VLBI measurements of different maser species obtained toward G009.62+00.20 E. The distribution of the maser cloudlets is superposed on the VLA maps at 7 mm, obtained with both the B and A configurations. Linear contouring was used for both maps starting from a 4σ level (Table 1); the first two negative levels fall below this threshold. Maser velocities along the line of sight are color coded according to the right-hand V_{LSR} scale.

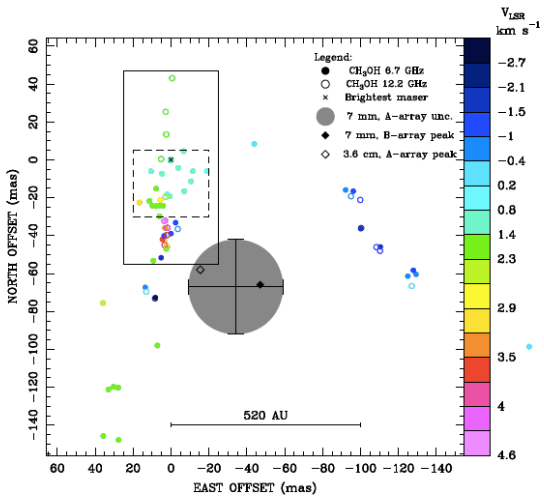

Figure 2. Close-up view of the 6.7 and 12.2 GHz (Sanna et al. 2009) maser emission arising within ~600 AU from the radio continuum peak. The 6.7 and 12.2 GHz masers are aligned by superposing their strongest features (cross) at zero offset. Maser velocities along the line of sight are color coded according to the right-hand V_{LSR} scale. The large gray circle gives the astrometric uncertainty of the radio continuum peak. The solid and dashed boxes mark the region of maser variability, and that studied in Figure 3, respectively. Linear scale at the bottom.

G009.62+00.20

- d~5.2 kpc
- 銀河的に最も明るい6.7GHzメタノールメーザー
- 244日の周期的なメタノールメーザーの増光

① VLA 7mm は2つのコンポーネント(E1, E2)

- 1300AU間隔

② E1から伸びる2つのメタノールメーザーリッジ

- E1から600AUに集中
- 6.7と12.2GHzで速度、位置が似ている

➢同じクラウドから出ている

45:The Environment of the Strongest Galactic Methanol Maser

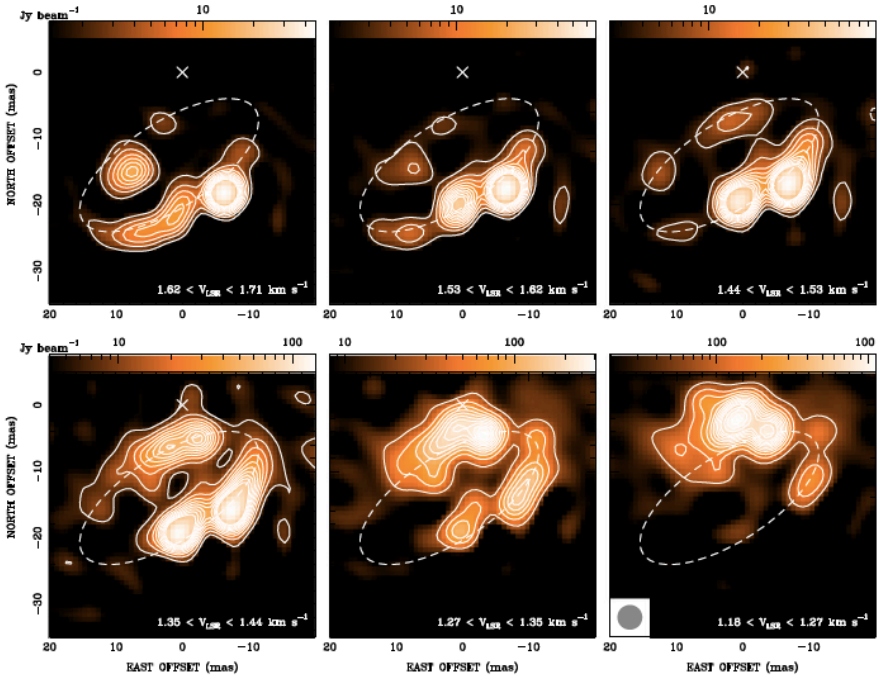

Figure 3. 6.7 GHz CH_3OH maser maps within ~150 AU south of the brightest CH_3OH maser (white cross). Each panel was obtained by summing the maser emission in three, consecutive, velocity channels (ranges in each bottom right corner). Contour levels start at 5σ and increase by 5σ steps for all panels but the two lower velocity maps which start at 10σ by 10σ steps. For each plot, the logarithmic color scale (upper wedge) range from a 3σ level up to the peak emission. The dashed ellipse marks the best fit to the overall maser emission. Restoring beam in the lower right panel.

③ 楕円状のメタノールメーザー

- ケプラー回転を示す
- 推定中心質量は7x10^(-3) Mo～8 Mjupiter

➢ 中心星はいない

④ 周期的増光の原因考察

➢ 成長中(Pulsational instability)の大質量YSOからのIR光がpumpingしている？

膨れた原始星がE2にいるとする
Inayoshi et al. 2013の原始星モデル
http://ads.nao.ac.jp/abs/2013MNRAS.431.3036I
E1を照らす光子量を見積もる

➢ この仮定で説明可能

➢ E2周辺のOHメーザーがE2にYSOがいることを示唆